Netherlands Journal of Geosciences

Original Article

Cite this article: Brouwer W.S. et al. 3D surface displacement estimation over the Groningen gas field, the Netherlands. *Netherlands Journal of Geosciences*, Volume 105, e13223. https://doi.org/10.70712/NJG.v105.13223

Received: 28 August 2025
Revised: 18 September 2026
Accepted: 18 September 2026
Published: 23 November 2026

Keywords:
decomposition; geodesy; Groningen; InSAR; surface displacements; strapdown

Corresponding author:
Ramon F. Hanssen,
Email: r.f.hanssen@tudelft.nl

© The Author(s), 2026. Published by the Netherlands Journal of Geosciences Foundation. This is an Open Access article, distributed under the terms of the Creative Commons Attribution licence (https://creativecommons.org/licenses/by/4.0/), which permits unrestricted re-use, distribution and reproduction, provided the original article is properly cited.

3D surface displacement estimation over the Groningen gas field, the Netherlands

Wietske S. Brouwer and Ramon F. Hanssen

Delft University of Technology, Delft, The Netherlands

Abstract

Since 1964, the Groningen gas field in the Netherlands has experienced significant subsidence due to gas extraction. Although satellite radar interferometry (InSAR) has been widely used to estimate the vertical displacements of the field, capturing the full three-dimensional deformation, including omnidirectional horizontal components, remained a challenge and has only been achieved from spatially sparse observations from ground-based geodetic stations. The recent development of the InSAR strapdown method suggests a solution to this problem. Yet, for an accurate decomposition, it is essential to isolate only scatterers representative of the deep gas-production-related deformation signal. Here we present a novel, data-driven approach that first disentangles the different deformation mechanisms present in the InSAR data. We then apply the strapdown method to decompose InSAR observations into vertical and directional horizontal displacement components, using frame orientation parameters estimated directly from the data. We incorporate uncontroversial contextual information and apply a bootstrapping method to enhance the quality of the results and propagate the uncertainty in the input data to provide quality metrics of the final estimates. Using this approach, we obtain reliable three-dimensional displacement estimates for the Groningen gas field, revealing previously unquantified horizontal displacements. Our results show that these horizontal displacements, especially close to the boundaries of the reservoir, are significant and must be considered alongside vertical motion to fully understand and mitigate the impacts of gas production.

Introduction

After production started in 1964, the Groningen gas field in the Netherlands has experienced significant pressure decline, resulting in subsurface compaction and surface displacements (subsidence) (Fokker et al., 2018). Since 2012, induced seismicity has caused over 250,000 damage reports and major societal consequences, including health issues and safety concerns (Schreuder et al., 2023; van der Lee, 2023; van der Voort & Vanclay, 2015). Monitoring surface displacements is therefore crucial – not only to improve understanding of subsurface processes, but also to support risk mitigation and damage assessment. Moreover, these measurements serve as critical input for inverse modelling efforts to estimate reservoir parameters such as pressure depletion and compaction (Kim, 2025; van Eijs & van der Wal, 2017; van Thienen-Visser & Fokker, 2017).

Surface displacements have been monitored since the start of gas production: initially with levelling surveys, and since 2003, increasingly with InSAR (Ketelaar, 2009; Ketelaar et al., 2006; Kim, 2025; NAM, 2015; van Thienen-Visser & Fokker, 2017; van Thienen-Visser et al., 2015). However, most studies focused on the vertical component, even though horizontal displacements can be expected – particularly near the field edges (Ketelaar, 2009; Ketelaar et al., 2020; Qin et al., 2019). Neglecting this component results in biased estimates of the vertical component and underutilises InSAR's full potential, since the observations capture both the vertical and horizontal deformation in the projection of the 3D displacement vector onto the satellite's line-of-sight (LoS) (Brouwer & Hanssen, 2023). Moreover, knowledge of the horizontal displacement gradients is crucial, as it provides information on compression, extension, shear, curvature, and tilt, which can affect infrastructure and buildings even more severely than vertical motion (Kratzsch, 1983).

However, the near-polar orbits and right-looking mode of most SAR satellites limit observations to two effective LoS directions, complicating a full 3D decomposition. Nonetheless, we argue that knowledge of the driving mechanism – gas extraction leading to a subsidence bowl (Geertsma, 1973; van Thienen-Visser et al., 2015) – enables using the strapdown method proposed by Brouwer and Hanssen (2024). The strapdown approach enables '2D-local/3D-global' solutions by using minimal and largely undisputed contextual information on the expected driving mechanisms and/or spatial geometry. It is a generic

method that defines a local reference system with transversal, longitudinal, and normal (TLN) axes, with displacement assumed to occur only in the transversal-normal plane. Applied to the Groningen case, this allows the LoS observations to be decomposed into normal (near-vertical) and transversal (inward, near-horizontal) components.

A fundamental requirement for the strapdown decomposition is that it utilises only observations that exclusively represent the deformation signal resulting from gas extraction, here referred to as the *deep* deformation signal. This poses a challenge, as InSAR observations reflect the *total* kinematic behaviour, which is the sum of the deep signal, the shallow subsurface signal and *autonomous* behaviour of objects and constructions, such as subsiding infrastructure, groundwater effects, or deforming buildings (NAM, 2020). Therefore, these signal components first need to be disentangled, before we can decompose the deep signal.

Here, we present a systematic approach to separating the deep deformation signal from shallow or autonomous surface motion. We first describe the classification methodology and present its results. Using only the InSAR observations classified as reflecting deep deformation, we then decompose the signal into local transversal and normal components, with orientations derived from iso-displacement lines in the viewing geometries. These components are subsequently resolved into three-dimensional east, north, and up components, using smoothness parameters estimated from well-constrained parts of the deformation field. Finally, we discuss the method and its results.

Scatterer classification: separating deep-only and mixed scatterers

To accurately decompose InSAR LoS observations into their normal and transversal components, it is crucial to include only those scatterers that uniquely represent the deformation mechanism of interest. In this case, the focus is on the subsidence bowl resulting from gas extraction at a reservoir located 3 km below the surface – referred to as the *deep* deformation signal, d_{deep}. Consequently, all InSAR scatterers are affected by this deep signal. Yet, many scatterers additionally exhibit displacement contributions due to (1) *shallow* processes and/or (2) *autonomous* movements, leading to a cumulative superposition of three distinct displacement components (Hanssen, 2001). Thus, the observed displacement signal[1] is

$$d_{\mathrm{obs}} = d_{\mathrm{shlw}} + d_{\mathrm{deep}} + d_{\mathrm{aut}} + n, \tag{1}$$

where n is a noise term, and the underline indicates the stochastic nature of the variable. Figure 1 shows an example of InSAR LoS data that is projected onto the vertical (PoV), shown for the province of Groningen (panel A). The colours represent the velocity of scatterers in mm/year, reflecting the total observed deformation behaviour. In panel A, the primary deep deformation signal – characterised by its spatial smoothness – is visible. Panels B, C, and D show additional deformation signals, including subsiding levees (B and C) and localised subsidence at the port of Eemshaven (D) (see also Figure 2). Including scatterers that are influenced by these *'non-deep'* deformation signals in the subsequent decomposition process (Section 3) would significantly bias the decomposition results. For instance, inadvertently attributing the levee-related deformation in panel C to gas extraction would lead to a significant overestimation of the normal displacement component. Therefore, it is essential to identify and exclude scatterers that display autonomous and/or shallow deformation. To address this, all scatterers will need to be classified into two mutually exclusive classes: the *deep-only* class and the *mixed* class. The deep-only class consists of a subset of scatterers, $u_{\mathrm{d/o}}$, that solely reflect the deep deformation signal, defined as

$$u_{\mathrm{d/o}}: d_{\mathrm{deep}} \in \mathbb{R} \wedge d_{\mathrm{shlw}} = 0 \wedge d_{\mathrm{aut}} = 0. \tag{2}$$

The '*mixed*' class contains the subset of scatterers influenced by a combination of deep, shallow, and autonomous signals, defined as

$$u_{\mathrm{mix}}: d_{\mathrm{deep}} \in \mathbb{R} \wedge d_{\mathrm{shlw}} \in \mathbb{R} \wedge d_{\mathrm{aut}} \in \mathbb{R}. \tag{3}$$

Consequently, we assume that all scatterers possess a deep component, though its numerical value may be zero. The proposed classification methodology comprises three subsequent steps and will be discussed below.

Step I: Quadrant classification

Given the detection of more than 1 million coherent point scatterers[2] in both ascending and descending Sentinel-1 acquisitions (see Table 1 for acquisition details), all points are initially classified as *mixed* by default (see Figure 4). We then use a quadtree approach to evaluate all scatterers in a quadrant and disentangle them into either the *deep-only* or the *mixed* class. A quadtree is a hierarchical data structure that recursively divides a region into four smaller quadrants, continuing this subdivision process until a predefined criterion or condition is satisfied (Finkel & Bentley, 1974; Samet, 1984). For each quadrant, we initially use the LoS velocities PoV direction (Brouwer & Hanssen, 2023). A plane is then fitted through these velocities to accommodate gradients in the displacement field, and consequently the residuals between the observations and the fitted plane are computed. If all scatterers within a quadrant reflect only the dominant deep deformation component, these residuals are expected to be relatively small, as the deep signal is assumed to be spatially smooth. However, a quadrant is further subdivided into four sub-quadrants if all of the following three criteria are met: (1) the spread of the residues between the LoS PoV observations and the fitted plane exceeds a specified threshold; (2) the quadrant contains more than N scatterers; and (3) the quadrant's size is larger than a predefined minimum. The latter two criteria ensure sufficient data density and statistical reliability within each quadrant.

An example of the resulting quadtree structure is shown in Figure 2. Starting with the large black quadrant (1), a plane is fitted through all PoV velocities. Because of the industrial area at the bottom right – a newly installed solar farm experiencing rapid initial consolidation – the PoV velocities cannot be sufficiently described by a single plane, and the residues between the observations and the plane will thus be large. Therefore, quadrant 1 will be subdivided into the four purple

1 Note that the displacement vector *d*, in mm, may also be interpreted as, e.g. an (average or instantaneous) displacement velocity in mm/y, since this is geometry-invariant.

2 We use the Delft taxonomy of scatterer classification proposed by Hu et al. (2019).

https://doi.org/10.70712/NJG.v105.13223

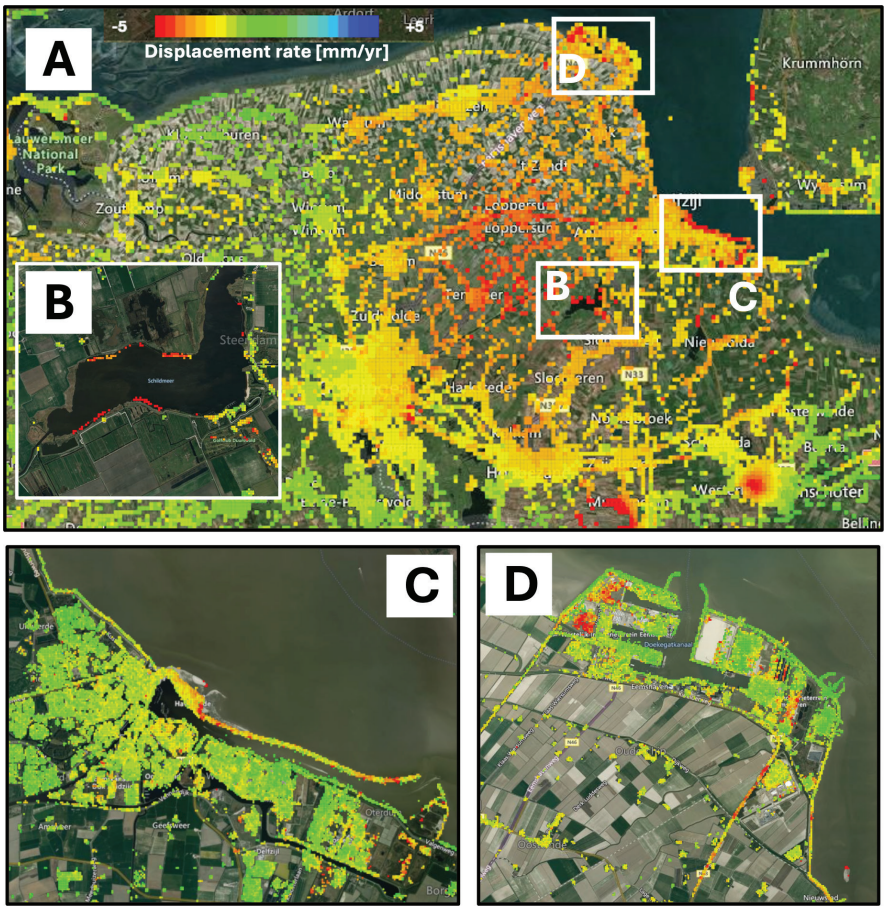

Figure 1. InSAR deformation velocities, derived from Sentinel-1 data, for the province of Groningen. The colours represent the average deformation velocity in the LoS direction projected onto the vertical direction, expressed in mm/year. Panel A shows the dominant, spatially smooth subsidence bowl resulting from gas extraction, with maximum velocities reaching up to 6.5 mm/yr at the centre. Due to the deep origin and large extent of the gas reservoir, all scatterers in the area are affected by the deep deformation signal, though its magnitude varies with location. Panels B, C, and D highlight localised autonomous deformation signals, such as subsiding dikes (B and C) and subsidence in the Eemshaven harbour (D). These autonomous signals are spatially less smooth compared to the widespread deep signal. LoS: line-of-sight.

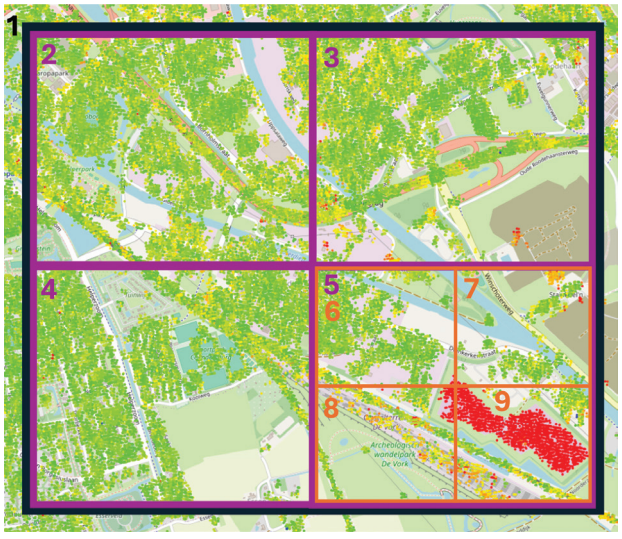

Figure 2. Example of quadrant classification, starting with the large black quadrant (1). Due to the additional subsidence signal in the bottom right (a newly installed solar farm), this quadrant is further subdivided into four new (purple) quadrants. Quadrants 2, 3, and 4 contain only one deformation phenomenon and will not be further subdivided, whereas quadrant 5 will be split into four new sub-quadrants. This way, areas exhibiting local shallow and autonomous signals are isolated from areas only representing the deep deformation signal.

Table 1. Acquisition details for Sentinel-1 tracks 15 and 37 in Groningen, the Netherlands.

Geometry/Date	S1 track 15	S1 track 37
Heading	Ascending	Descending
Mean θ	36.1°	36.9°
Mean α_d	259.3°	100.5°
Start	2 February 2015	2 December 2015
End	21 June 2023	5 July 2023

quadrants, after which this process will be repeated. The residues with fitted planes in sub-quadrants 2, 3, and 4 are small – here we use an upper threshold of 1.5 mm/yr for the standard deviation of the residues – and will not be further subdivided. The fifth quadrant is further subdivided into the four orange ones. Thus, the presence of local autonomous or shallow signals requires smaller quadrants to describe the signal.

After this procedure, the quadrants (and thus all scatterers within them) are classified into the two disjunct classes: deep-only and mixed. Under the assumption that the deep signal is spatially smooth, we classify a quadrant as *deep-only* if (1) it is large (>700 m), (2) the dispersion (σ) of the residuals of the scatterers with the estimated plane is small (i.e. <1.5 mm/y), and (3) the gradient of the fitted plane is low

https://doi.org/10.70712/NJG.v105.13223

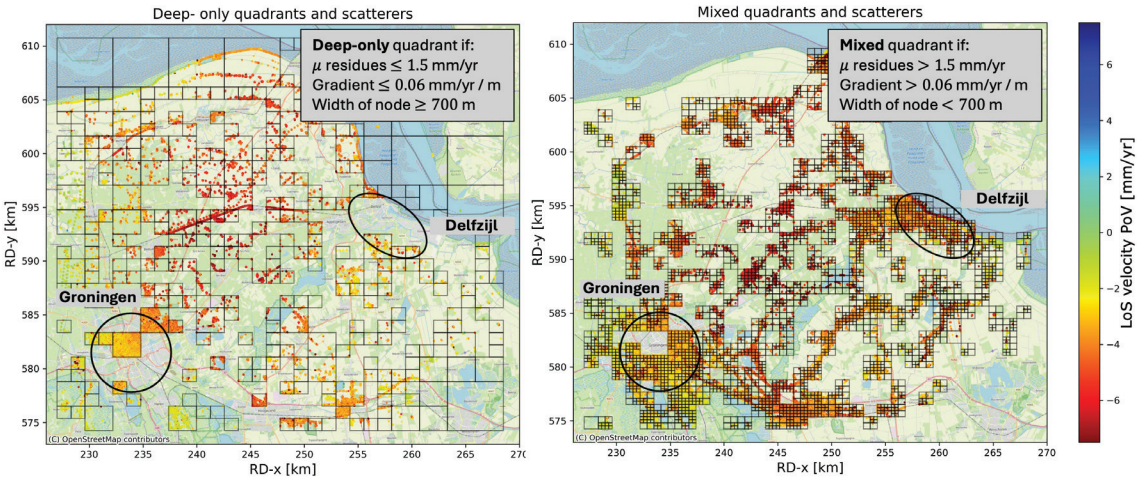

Figure 3. A result of the separation of quadrants into either *deep-only* (left) or *mixed* (right). Large quadrants, where the residues with the fitted plane through the PoV velocities are small, are assigned to the deep-only class. Local deformation phenomena, such as subsiding infrastructure, require smaller quadrants to describe the deformation behaviour and are assigned to the mixed quadrants. Note that both panels are mutually exclusive. PoV: projected onto the vertical.

(i.e. <0.06 mm/y/m).[3] The result for the ascending dataset is shown in Figure 3, where the left panel shows the deep-only quadrants and scatterers, and the right panel the mixed ones, respectively.

At this point, all scatterers located within a given quadrant inherit a uniform classification label, depending on the classification of the quadrant. For the Groningen case, the percentage of scatterers per class is presented in the flowchart in Figure 4, where the orange and the blue values represent the ascending and descending acquisitions, respectively. Indeed, the majority of scatterers is classified as *mixed*. However, some scatterers in *deep-only* quadrants may still exhibit additional autonomous and/or shallow behaviour, and some scatterers in *mixed* quadrants may only exhibit a deep signal. This is addressed below in Steps II and III.

Step II: Point reclassification deep-only to mixed

Individual scatterers in *deep-only* quadrants may actually still exhibit additional autonomous and/or shallow behaviour. To detect potential scatterers belonging to the mixed class, we analysed the histograms of the PoV velocities in the deep-only quadrants. If all scatterers represent the same deformation signal, the histogram is expected to be symmetrical, only representing random noise. However, if additional deformation components are present with significant magnitudes, the histogram may become skewed. As gravity is the main driving force (i.e. points will more often move systematically down than up), we specifically expect a left-skewed distribution. Additionally, since *all* scatterers are affected by the deep driving mechanisms, while only a smaller subset may have additional components, we assume that the main mode of the histogram corresponds to the deep-only deformation signal.

3 The chosen maximum value of 700 m is ~20% of the reservoir depth, which is 3 km. The maximum sigma value for the residuals was chosen to be 1.5 mm/yr, as we expect to see larger values when autonomous motion takes place. The maximum gradient was chosen one order of magnitude larger (to be conservative) than we estimated at the LoS data near the edges of the field. Note that all values are application dependent.

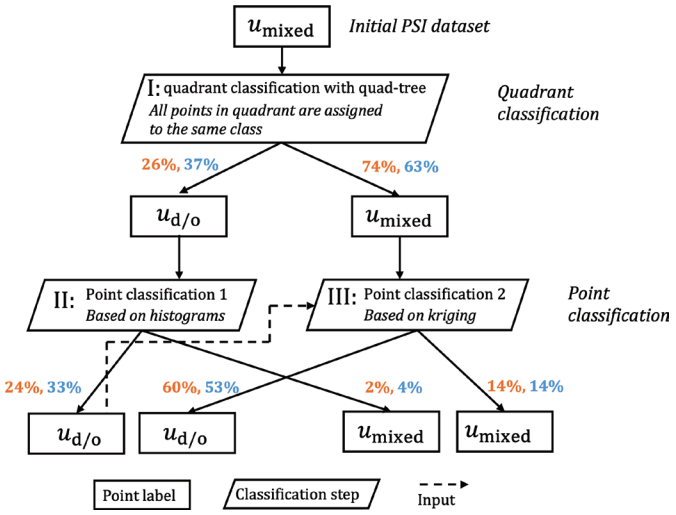

Figure 4. Flowchart of the classification procedure: in the first step of the classification process, the quadrants and all scatterers within them are classified into two classes. After quadrant classification, scatterers may erroneously be classified. In the first point classification step, we analyse the histograms of the deep-only labelled scatterers and reclassify the mixed scatterers that were erroneously classified as deep-only. In the second classification, we use information from the deep-only classified scatterers to predict the deep deformation component at the mixed scatterers. We use this information to reclassify the erroneously classified mixed scatterers to deep-only. The percentages in red and blue represent the proportion of scatterers belonging to a class for ascending and descending acquisitions, respectively.

When fitting a skew-normal distribution to all velocities within a quadrant, we subsequently estimate the main mode of all velocities and their Median Absolute Deviation (MAD).[4] We reclassify scatterers with velocities outside the range (main mode ± 2MAD) to *mixed*, following the procedure of Hanssen and van Leijen (2017). An example is shown in Figure 5a, where two deformation mechanisms are present: a gas production facility and the railway in the south, clearly visible in the skewed histogram. Consequently, all scatterers within the selected range are labelled as deep-only, while the remaining scatterers in the left tail are classified as mixed (see Figures 5c and 5d).

4 Similar to the mode being less influenced by outliers than the mean, the MAD is less influenced by the sample size (Huber, 2011).

https://doi.org/10.70712/NJG.v105.13223

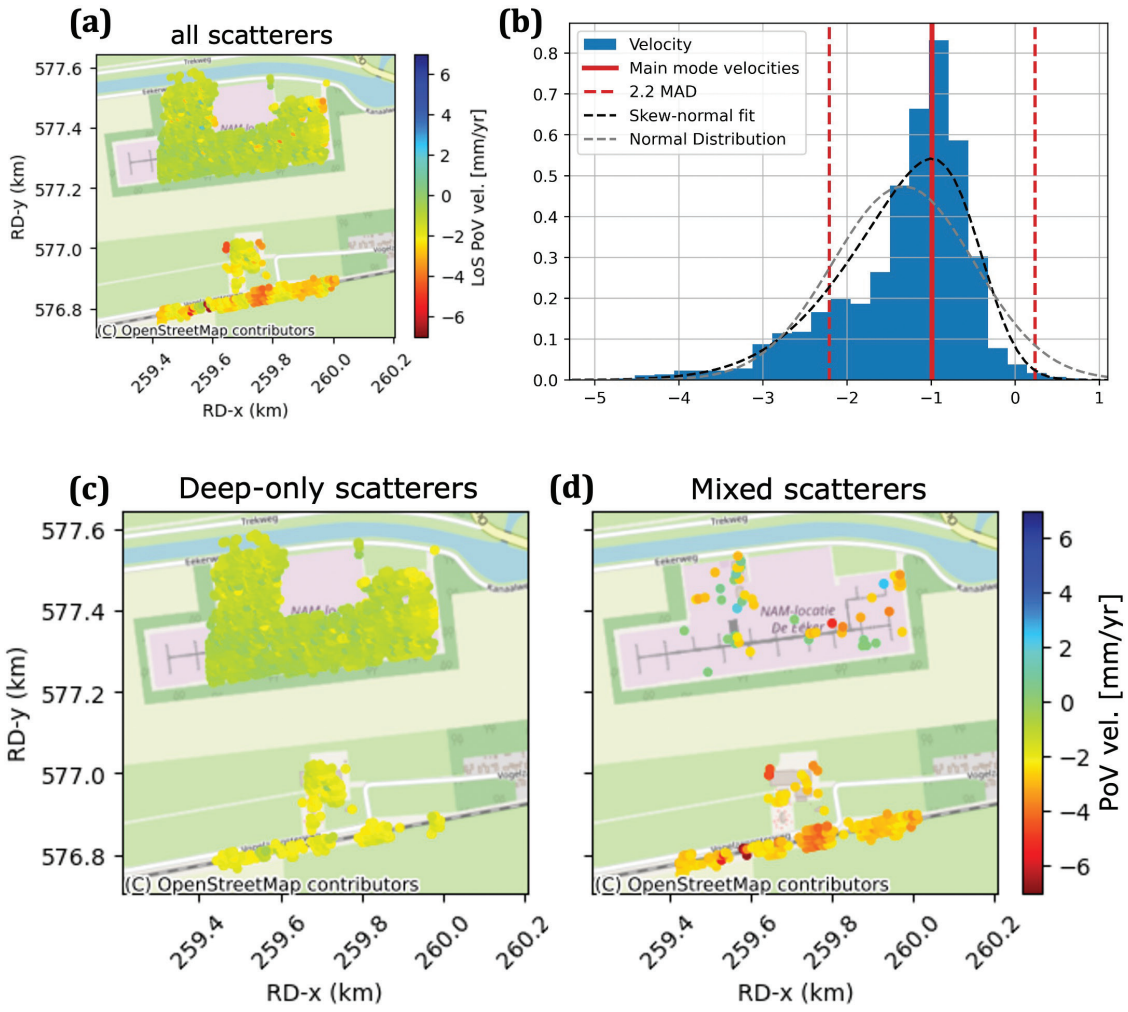

Figure 5. In deep-only quadrants, individual scatterers actually belonging to the mixed class should be detected and reclassified. (a) shows the PoV velocities of all scatterers in such a quadrant, while (b) presents the corresponding histogram. The skewness of the histogram indicates the presence of multiple deformation components. The solid red line marks the main mode velocity, and the dashed red lines indicate the (main mode ± 2 × MAD) range. Scatterers outside this range are reassigned to the mixed class (d), while the remaining scatterers are individually classified to the deep-only class (c). PoV: projected onto the vertical; MAD: Median Absolute Deviation.

Step III: Point reclassification mixed to deep-only

After the quadrant classification in Step I, some individual scatterers in mixed quadrants may actually be representing *deep-only* signals. Identifying those scatterers is important to achieve sufficient spatial point density required for the subsequent geometric decomposition (see Figure 3). For example, Figure 3a shows a lack of deep-only scatterers in the cities of Groningen (southwest) and Delfzijl (east), despite the expectation of finding such scatterers in these areas. Without deep-only scatterers at these locations, a decomposition cannot be performed.

For this 'Step III' reclassification (see Figure 4), we include the deep-only scatterers that were the result of Step II. The assumption is that for those scatterers the autonomous and shallow deformation components are zero, i.e. $d_{\mathrm{aut}} = d_{\mathrm{shlw}} = 0$, and therefore $d_{\mathrm{obs}}(u_{d/o}) = d_{\mathrm{deep}}(u_{d/o}) + n$, where $u_{\mathrm{d/o}}$ identifies a deep-only labelled scatterer. This deep-only signal is expected to exhibit a certain spatial smoothness, which we will use to predict the deep signal at locations of the scatterers that were labelled as mixed, i.e. u_{mix}, after Step I. We use ordinary kriging interpolation with

$$\hat{d}_{\mathrm{deep}}(u_{\mathrm{mix}}) = \sum_{i=1}^{n} \lambda_i d_{\mathrm{obs}}(u_{i,\mathrm{d/o}}), \tag{4}$$

where $d_{\mathrm{obs}}(u_{\mathrm{i,d/o}})$ represents the observed PoV velocities of the *deep-only* classified scatterers, n is the number of deep-only classified scatterers, and λ_i are the kriging weights derived from the variogram corresponding to the deep deformation signal.

The variogram is derived from the observed LoS deformation that is PoV of the *deep-only* classified scatterers, which would therefore contain both noise and the deep signal.

We fit a Gaussian model through the data, with estimated variogram parameters as presented in Table 2. The parameters for the ascending and descending datasets are comparable, with slight differences possibly due to the different viewing geometry.

The kriging interpolation provides a prediction of the deep signal at the locations of the mixed scatterers, here denoted as $\hat{d}_{\mathrm{deep}}(u_{\mathrm{mix}})$. Comparing the predicted deep signal with the observed signal, we estimate the concatenated autonomous and shallow behaviour of the scatterer with

https://doi.org/10.70712/NJG.v105.13223

Table 2. Gaussian variogram parameters estimated from the descending and ascending PoV values used for the kriging interpolation in Section 2.3.

Range (km)	Nugget (mm²/y²)	Sill (mm²/y²)
asc 16	0.2	3
desc 17	0.3	4

This shows that both viewing geometries result in comparable variogram parameters. PoV: projected onto the vertical.

$$\hat{d}_{\text{aut}}(u_{\text{mix}}) + \hat{d}_{\text{shlw}}(u_{\text{mix}}) = d_{\text{obs}}(u_{\text{mix}}) - \hat{d}_{\text{d/o}}(u_{\text{mix}}). \quad (5)$$

If the absolute value of $\hat{d}_{\text{aut}}(u_{\text{mix}}) + \hat{d}_{\text{shlw}}(u_{\text{mix}})$ is small, we assume that the observed deformation signal only has a deep component and reclassify those scatterers from the mixed class to the deep-only class. As a practical limit, here we reclassify *mixed* scatterers into the *deep-only* class when $|\hat{d}_{\text{aut}}(u_{\text{mix}}) + \hat{d}_{\text{shlw}}(u_{\text{mix}})| < 1.5$ mm/y (see footnote 3) to avoid excessive smoothing and to allow for some missed signals. This value was chosen since it is equal to the threshold of the spread of the residues to separate deep-only and mixed quadrants in Section 2.1 (Step I). When $|\hat{d}_{\text{aut}}(u_{\text{mix}}) + \hat{d}_{\text{s}}(u_{\text{mix}})| \geq 1.5$ mm/y, the scatterer remains a mixed scatterer, but with (1) a disentangled deep component and (2) a concatenated autonomous/shallow component, which can be used for other studies. The result of this three-step approach is a non-overlapping classification of *deep-only* and *mixed* scatterers, whose estimated PoV velocities are shown in Figure 6.

A comparison between Figures 3 and 6 reveals that the spatial distribution of deep-only classified scatterers has significantly improved.

From the original 74% of point scatterers classified as *mixed* after Step I (see Figure 4) about 80%[5] are ultimately moved to the deep-only class in Step III. This shows that the two subsequent point classification steps (II and III) are effective and necessary. The high percentage of reclassified scatterers in Step III is likely caused by the large number of scatterers in the cities of Delfzijl and Groningen. Initially, almost all scatterers in those cities were classified as mixed.

Discussion

The proposed classification method separates deep-only and mixed scatterers based on the expected smoothness of the deep signal, and does not require direct physical knowledge of the nature of the scatterers. While these expectations and assumptions may be somewhat heuristic, they are explicitly stated and therefore subject to scrutiny. Importantly, in this study our goal is not to obtain a detailed characterisation of autonomous or shallow scatterer behaviour. Instead, we aim to remove scatterers exhibiting such motion from the dataset as effectively as possible prior to decomposition. The decomposition process depends on identifying 'regions of uniform motion' (RUMs) (Brouwer & Hanssen, 2024), within which velocities are averaged. As a result, any misclassification – such as incorrectly labelling a mixed scatterer as deep-only – is likely to be attenuated within these regions. As shown in Figure 4, in the end approximately 85% of scatterers are classified as deep-only, with only 15% identified as mixed. This indicates that the method does not excessively smooth the data.

5 60 / (60 + 14) = 81% (ascending) and 53 / (53 + 14) = 79% (descending).

Decomposing deep deformation into vertical and directional horizontal components

Working only with the resulting *deep-only* scatterers in both the ascending and descending datasets, we can decompose the LoS observations into normal and transversal components using the strapdown method, as proposed by Brouwer and Hanssen (2024). This uses a local Cartesian coordinate system with TLN components, where the displacements occur only in the transversal-normal plane by definition. The frame's orientation is defined by three angles: Λ, Φ, and Ω, where $\Lambda \in [0°, 360°)$ is the azimuth of the longitudinal direction relative to the geographic north, $\Phi \in (-90°, +90°]$ is the elevation angle of the longitudinal direction relative to the horizontal, and $\Omega \in (0°, +90°]$ is the elevation angle of the transversal direction, using the sign conventions proposed by Brouwer and Hanssen (2024).

For subsidence bowls, the normal direction is approximately vertical, while horizontal displacements are expected to be directed toward the centre of the bowl, i.e. the longitudinal direction is aligned parallel to the iso-deformation lines, and the transversal direction is near-centripetal.

With the LoS observations from an ascending, $\underline{d}^{\text{asc}}_{\text{LoS}}$, and descending acquisition, $\underline{d}^{\text{asc}}_{\text{LoS}}$, the transversal and normal displacements, d_T and d_N can be solved from a nonlinear set of observation equations with

$$E\{\underbrace{\begin{bmatrix} \underline{d}^{\text{asc}}_{\text{LoS}} \\ \underline{d}^{\text{dsc}}_{\text{LoS}} \\ \underline{\Lambda} \\ \underline{\Omega} \\ \underline{\Phi} \end{bmatrix}}_{\underline{y}}\} = \underbrace{\begin{bmatrix} P_T^{\text{asc}}(\Lambda,\Omega,\Phi)d_T + P_N^{\text{asc}}(\Lambda,\Omega,\Phi)d_N \\ P_T^{\text{dsc}}(\Lambda,\Omega,\Phi)d_T + P_N^{\text{dsc}}(\Lambda,\Omega,\Phi)d_N \\ \Lambda \\ \Omega \\ \Phi \end{bmatrix}}_{A(x)}, \text{ and} \quad (6)$$

$$D\{\underbrace{\begin{bmatrix} \underline{d}^{\text{asc}}_{\text{LoS}} \\ \underline{d}^{\text{dsc}}_{\text{LoS}} \\ \underline{\Lambda} \\ \underline{\Omega} \\ \underline{\Phi} \end{bmatrix}}_{\underline{y}}\} = \underbrace{\begin{bmatrix} Q_{\text{LoS,asc}} & 0 & 0 & 0 & 0 \\ 0 & Q_{\text{LoS,asc}} & 0 & 0 & 0 \\ 0 & 0 & \sigma^2_{\Lambda} & 0 & 0 \\ 0 & 0 & 0 & \sigma^2_{\Omega} & 0 \\ 0 & 0 & 0 & 0 & \sigma^2_{\Phi} \end{bmatrix}}_{Q_{yy}}, \quad (7)$$

where

$P_T = (\sin\theta \sin\alpha_d \cos\Lambda - \sin\theta \cos\alpha_d \sin\Lambda)\cos\Omega -$
$(-(\sin\theta \sin\alpha_d \sin\Lambda + \sin\theta \cos\alpha_d \cos\Lambda)\sin\Phi +$
$\cos\theta \cos\Phi)\sin\Omega$ and
$P_N = (\sin\theta_m \sin\alpha_d \cos\Lambda - \sin\theta \cos\alpha_d \sin\Lambda)\sin\Omega +$
$(-(\sin\theta_m \sin\alpha_d \sin\Lambda + \sin\theta \cos\alpha_d \cos\Lambda)\sin\Phi +$
$\cos\theta \cos\Phi)\cos\Omega$.

$E\{.\}$ expresses the expectation of the model, and $x = [d_T, d_N, \Lambda, \Omega, \Phi]^T$ is the vector of unknowns. In the model, $\underline{d}^{\text{asc}}_{\text{LoS}}$ and $\underline{d}^{\text{asc}}_{\text{LoS}}$ are 'sets' of LoS observations, i.e. all LoS observations for one viewing geometry over a RUM (see Brouwer and Hanssen 2024 for further details). The first two rows of A(x) are unique nonlinear equations of x due to the difference in viewing geometry between ascending and descending orbits, defined by the incidence angle towards the radar, θ, and the azimuth of the zero-Doppler plane (ZDP) at the target position towards the satellite, α_d. To resolve the rank deficiency, pseudo-observations

https://doi.org/10.70712/NJG.v105.13223

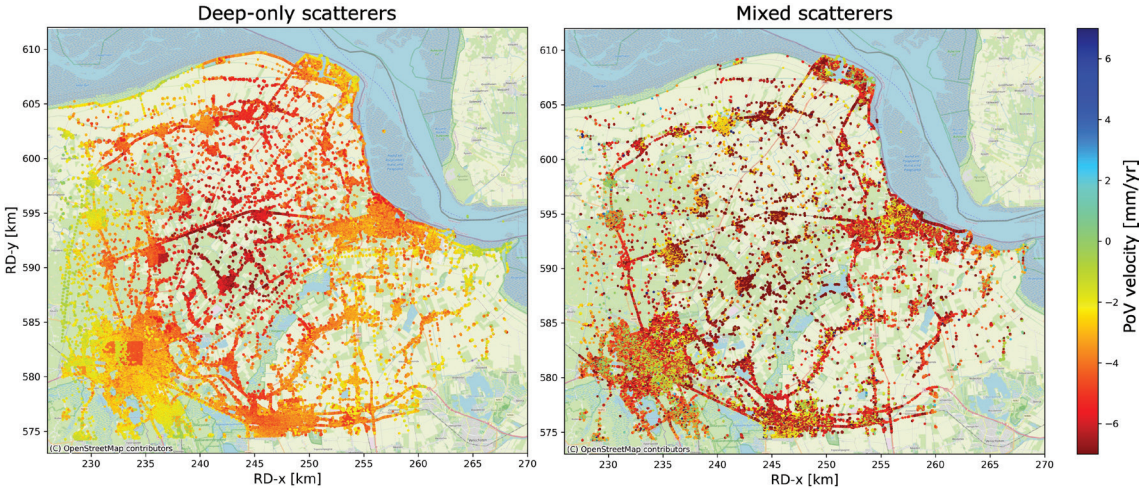

Figure 6. Final result for the classification of scatterers into two disjunct sets of points: *deep-only* (left) and *mixed* (right) for a Sentinel-1 ascending acquisition over Groningen. Both figures share the same colour scale shown on the right. Note that the mixed scatterers also represent the deep deformation behaviour. It can be seen that the deep-only scatterers show a smoother signal in space.

for $\underline{\Lambda}$, $\underline{\Omega}$, and $\underline{\Phi}$ are added to the system. These pseudo-observations are also used as initial values in Equation (6) and are based on best-effort estimates for the frame orientation, as discussed below. $D\{.\}$ is the dispersion of the observations, where Q_{LoS} is the covariance matrix of the LoS observations for a set. This covariance matrix is a diagonal matrix containing the variances of displacements for each scatterer within the set. The uncertainty in the orientation of the TLN frame is represented in σ^2_{Λ}, σ^2_{Ω}, and σ^2_{Φ}, values that reflect the degree of uncertainty in the orientation of the frame. The alignment of the local frame with respect to the local deformation phenomena is a key part of the method, ensuring that displacements occur exclusively in the transversal-normal plane and that the alignment uncertainty is realistically (i.e. conservatively) approximated, to obtain realistic quality metrics for the final displacement estimates.

The nonlinear model of observation equations, i.e. Equations (6) and (7), can be solved using iterative techniques such as the Gauss-Newton method. This process requires linearising the system of equations and providing initial approximations for the unknown parameters $x[0]$, i.e. Λ, Φ, Ω, d_T and d_N. Below we (1) discuss how the initial values are derived for the Groningen gas field, and (2) perform the strapdown decomposition, resulting in estimates for the normal and transversal components. As the quality of the estimated transversal components varies with orientation, we (3) further improve the quality of the estimates based on uncontroversial contextual information.

Approximating the orientation of the TLN frame

The subsidence signal of the Groningen gas field is notably non-circular (see Figure 6a), which makes accurately estimating the TLN frame orientation important. The LoS observations are PoV for both viewing geometries to obtain a rough first-order approximation of the gradients of the subsidence field. Figures 7a and b show the kriging predictions of the PoV velocities for both acquisitions, together with estimated contour lines. It can be seen that, due to the presence of a horizontal component, the contour lines for both datasets differ slightly. We compute the mean value of these two fields (see Figure 7c) to get an initial approximation of the shape of the field with

$$\hat{\underline{d}}_{\mathrm{PoV}} = \frac{1}{2}(\hat{\underline{d}}_{\mathrm{PoV,asc}} + \hat{\underline{d}}_{\mathrm{PoV,dsc}}) \tag{8}$$

where $\hat{\underline{d}}_{\mathrm{PoV,asc}}$ and $\hat{\underline{d}}_{\mathrm{PoV,dsc}}$ are the two kriging predictions for a regular grid, and $\hat{\underline{d}}_{\mathrm{PoV}}$ is the mean estimated field. Here, the PoV values are expressed as positive subsidence rates: greater values correspond to greater subsidence, and the field attains its maximum at the bowl centre. The spatial gradient of this mean field is

$$\nabla\hat{\underline{d}}_{\mathrm{PoV}} = \left(\frac{\partial\hat{\underline{d}}_{\mathrm{PoV}}}{\partial x}, \frac{\partial\hat{\underline{d}}_{\mathrm{PoV}}}{\partial y}\right) = (d_x, d_y), \tag{9}$$

where x and y denote the east and north directions respectively, and points in the direction of steepest *increase* of the subsidence field. This gradient is directed centripetally and coincides with the transversal direction T of the TLN frame. The azimuth of the transversal axis (measured clockwise from north) is therefore

$$\alpha_T = \mathrm{atan2}(d_x, d_y) \bmod 2\pi, \tag{10}$$

where atan2(d_x, d_y) uses the azimuth convention, with the east component as the first argument and the north component as the second. The longitudinal axis L is by definition perpendicular to T and the azimuth of the longitudinal axis is therefore

$$\Lambda = \left(\alpha_T + \frac{\pi}{2}\right) \bmod 2\pi = \left(\mathrm{atan2}(d_x, d_y) + \frac{\pi}{2}\right) \bmod 2\pi. \tag{11}$$

Figure 7c shows the mean contour lines together with the estimated transversal directions as black arrows, which are perpendicular to the contour lines and point towards the bowl centre.

The frame alignment also requires estimates for Ω and Φ; because of the absence of significant topography in this region, we use $\Omega = 0°$ and $\Phi = 0°$.

https://doi.org/10.70712/NJG.v105.13223

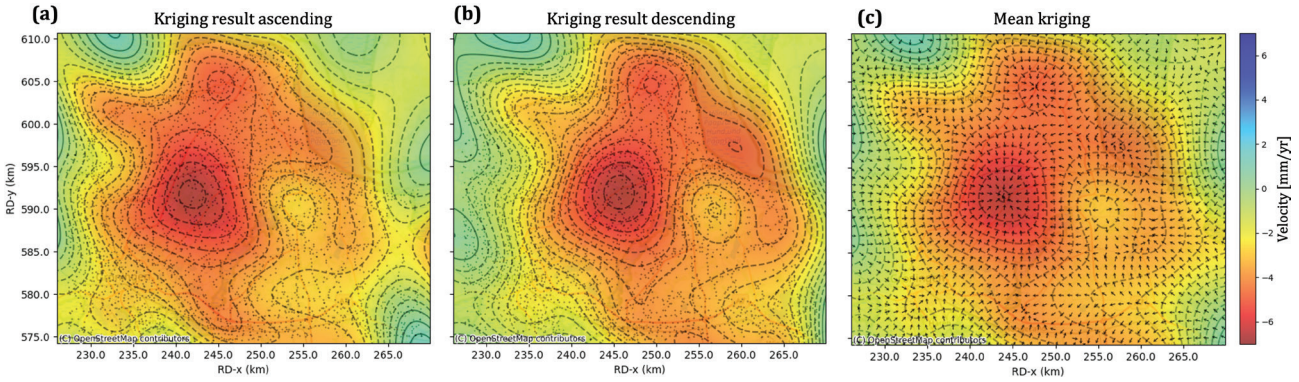

Figure 7. (a) and (b): kriging predictions of ascending and descending *deep-only* PoV velocities on a regular grid with a 200 m resolution. Black dots indicate the locations of the input data, which are (a representative subset of) *deep-only* classified scatterers. A random spatial subset of points is used to reduce the computational load of the kriging estimation. The subset was chosen to ensure good spatial coverage, with points evenly distributed across the area. Due to the presence of a horizontal component, the maximum subsidence occurs at a different location for both acquisitions. (c): mean of the two fields shown in (a) and (b), along with contour lines and the estimated orientation of the transversal axes as vectors, assumed to be perpendicular to the contour lines. PoV: projected onto the vertical.

Strapdown decomposition

Using the approximated frame orientation, we decompose the LoS deep-only observations for RUMs – areas where all selected deep-only scatterers are assumed to exhibit the same displacement behaviour (Brouwer & Hanssen, 2024). We divide the province of Groningen into grid cells of 500 × 500 m, and estimate the mean and the standard deviation of the LoS velocity per grid cell, where the latter serves as an approximation for Q_{LoS} in Equation (7). We conservatively set $\sigma_{\Lambda} = 15°$, to account for imperfections in our initial estimate of the frame orientation, and $\sigma_{\Omega} = \sigma_{\Phi} = 5°$. The nonlinear system of observation Equations (6) and (7) is solved using a Gauss-Newton iteration scheme, which requires initial estimates for the unknown parameters. We set $d_T^{[0]} = d_N^{[0]} = 1$ mm/yr (as we assume that the deep signal is present everywhere), $\Omega^{[0]} = \Phi^{[0]} = 0°$, and use the computed values from Section 3.1 for $\Lambda^{[0]}$.

Figures 8a and 9a show the estimated velocities for the normal and transversal components, respectively, together with corresponding sigma values in Figures 8f and 9f. It shows that the magnitude of the estimated normal component is consistent with the estimated contour lines that serve as input for the TLN frame orientation (the contour lines are shown in the figures as a reference). As an additional check on the viability of the approximated TLN frame orientation, we recompute new contour lines based on $\hat{d}_N$ (see Figure 10). This shows that the orientation of the contour lines matches well, with only some minor deviations on the west side of the field. When we derive new estimates for Λ from these new contour lines and look at the difference, we find a mean value of 0.1 degrees and a σ value of 8 degrees. Note that these values are small compared to the a priori conservative assumption of $\sigma_{\Lambda} = 15°$. The estimated normal component reaches values of up to −6.5 mm/yr in the middle of the field, at RD coordinates [244,000, 592,000], north of the city of Ten Post, which is well in line with earlier results (NAM, 2020). Also, a steeper gradient in the estimated normal velocities at the edges of the field is observed.

The estimated values for the transversal component (see Figure 9a) predominantly show positive (blue) values, which confirms that the estimated frame orientation seemed appropriate. As expected, higher transversal velocities are observed at locations where the contour lines are closer together – particularly around the city of Groningen, indicated with the circle between x-coordinates 230–240 km and y-coordinates 585–595 km. Here, transversal velocities of up to 1.8 mm/yr are estimated, which, given that gas extraction has been ongoing since 1960, would result in approximately 11 cm of cumulative horizontal displacement.

Extreme values for the transversal velocity and large corresponding standard deviations are observed for RUMs where the transversal direction is (almost) aligned with the north direction (see Figure 9e). At these RUMs, the transversal direction is close to the orientation of the null line,[6] resulting in an ill-posed problem. Consequently, those unknowns can be estimated with low precision, also affecting the normal component. Below, we address and reduce these adverse effects.

Improvement using contextual premises

As we are analysing a deformation signal known to be caused by gas extraction from a reservoir at a depth of 3 km, the estimated extreme transversal velocities shown in Figure 9a are physically unrealistic. Note that the colour bar is clipped for visualisation purposes, but we observed estimated values beyond ±10 mm/yr. In fact, (1) the depth of the reservoir is expected to result in a spatial displacement signal with some degree of spatial smoothness in the tangential direction, i.e. roughly parallel to the iso-displacement lines approximated in Figure 7c. While this degree of smoothness may differ slightly depending on the sectorial position, there is (2) no reason that the transversal displacement gradients are as strong as the observed ones in Figure 9a. Instead, (3) it is very likely that the extreme values are a consequence of the lower sensitivity in those sectorial positions. Fortunately, (4), the sensitivity to estimate the transversal displacement gradients in the other sectorial positions is very high.

We consider (1) to (4) as '*contextual premises*', i.e. statements assumed to be true, but formulated explicitly to

6 The null line is the direction in three-dimensional space in which no displacements can be observed by both the ascending and descending acquisitions. Its orientation can be computed from the viewing geometry of the ascending and descending acquisitions and is described by azimuth ϕ and elevation angle ζ; see Brouwer and Hanssen (2023).

https://doi.org/10.70712/NJG.v105.13223

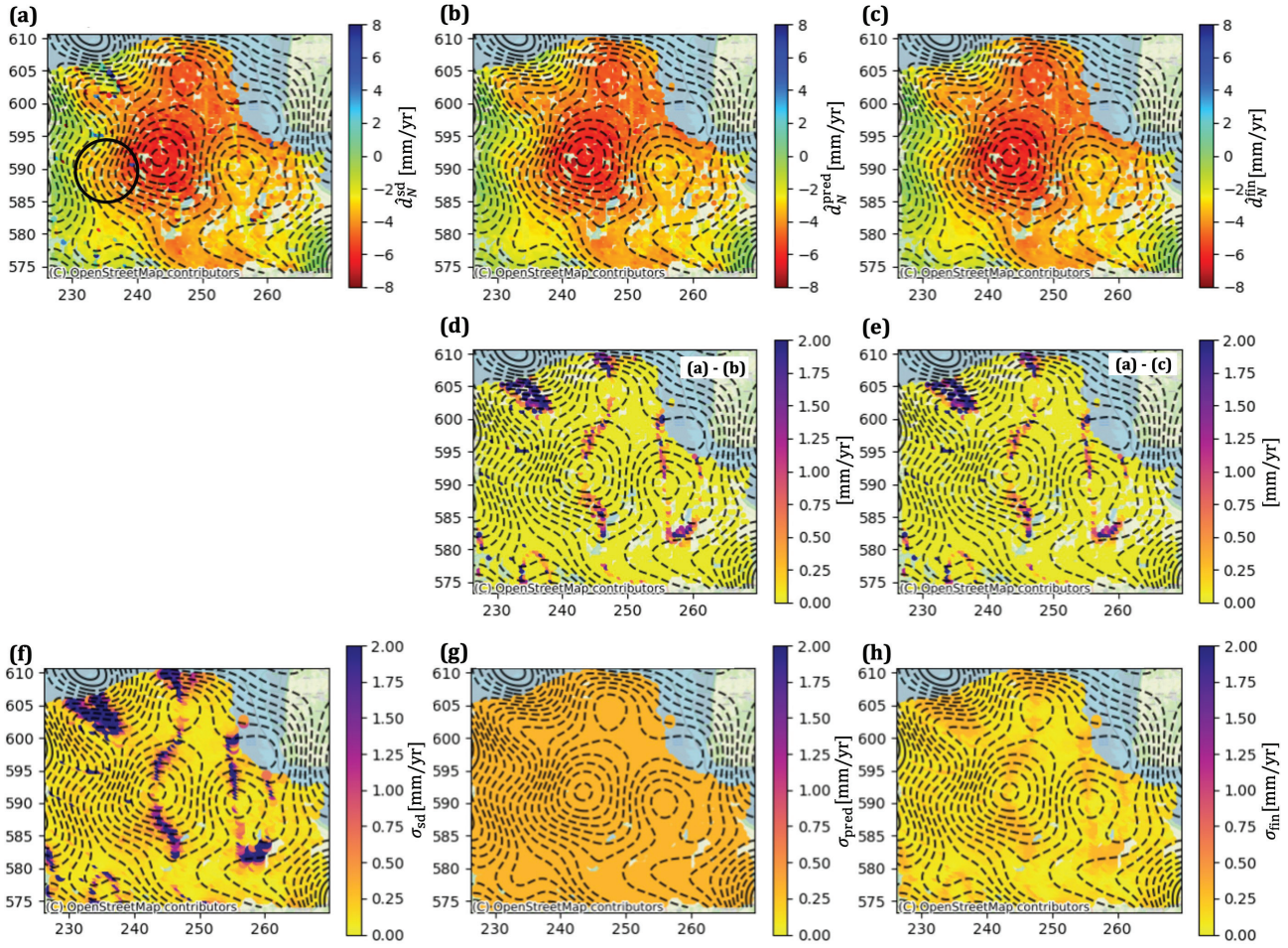

Figure 8. (a) Normal velocities estimated using only the strapdown decomposition, with the corresponding quality values (σ) shown in (f). (b) presents the results obtained via kriging interpolation, $\hat{d}_N^{\text{pred}}$, with corresponding sigmas in (g), and the difference with the strapdown results in (d). In (c), we show the combined estimates for the normal component, $\hat{d}_N^{\text{fin}}$, derived by solving the mathematical model from Equations (13) and (14), with the associated σ values shown in (h), and the difference with the strapdown solution in (e). Notably, the combined approach improves the quality of the estimates – particularly for RUMs where the transversal direction aligns with the north–south direction; see the lower sigma values of (h) compared to (f). The circle in (a) locates the city of Groningen. RUM: region of uniform motion.

allow for scrutiny and potential refutation. Deductively, it follows from the premises that the results from the 'transversal-sensitive' RUMs, i.e. with well-solvable displacement estimates, provide insight into the degree of smoothness of the transversal deformation signal, also over the sectorial positions with transversal-less-sensitive RUM's. We can use this approach to weigh the kinematic estimates from Section 3.2 and combine them with smoothness conditions derived from other parts of the field. We apply this approach subsequently to the normal and to the transversal component of the velocity.

Normal component

In order to quantify the smoothness, we compute the variogram of the normal velocity using the strapdown estimates of only well-solvable RUMs, i.e. RUMs where the direction of the transversal component is at least 15 degrees away from the orientation of the null line,[7] which has an elevation and azimuth angle of $\zeta = 7.8°$ and $\phi = 0.0°$, respectively. The resulting variogram, shown in Figure 11a, is an approximation of the signal's smoothness. Since the variogram is based on velocities from the strapdown decomposition, it has a non-zero nugget to account for imperfections in the decomposed results. We fitted a Gaussian variogram model with a range of 18.5 km, a nugget of 0.1 mm²/yr², and a sill of 2.3 mm²/yr². The variogram values are the kriging weights used to predict a new normal velocity based on the expected smoothness of the signal, for each RUM, using

$$\hat{d}_N^{prod} = \sum_{i=1}^{n} \lambda_i \hat{d}_N^{sd}, \tag{12}$$

where I is the identifier of a RUM that is at least 15 degrees away from the orientation of the null line, $\hat{d}_N^{\text{sd}}$ is the normal displacement velocity from the strapdown decomposition, and λ are the kriging weights derived from the variogram model. In this way, we predict a new normal velocity for all RUMs, based solely on the RUMs for which the strapdown estimates were reliable. This results in two normal displacement velocity estimates per RUM, $\hat{d}_N^{\text{sd}}$ and $\hat{d}_N^{\text{pred}}$, each with an associated variance. The final estimate for the normal component is then obtained by combining these values through the following mathematical model

7 See footnote 6.

https://doi.org/10.70712/NJG.v105.13223

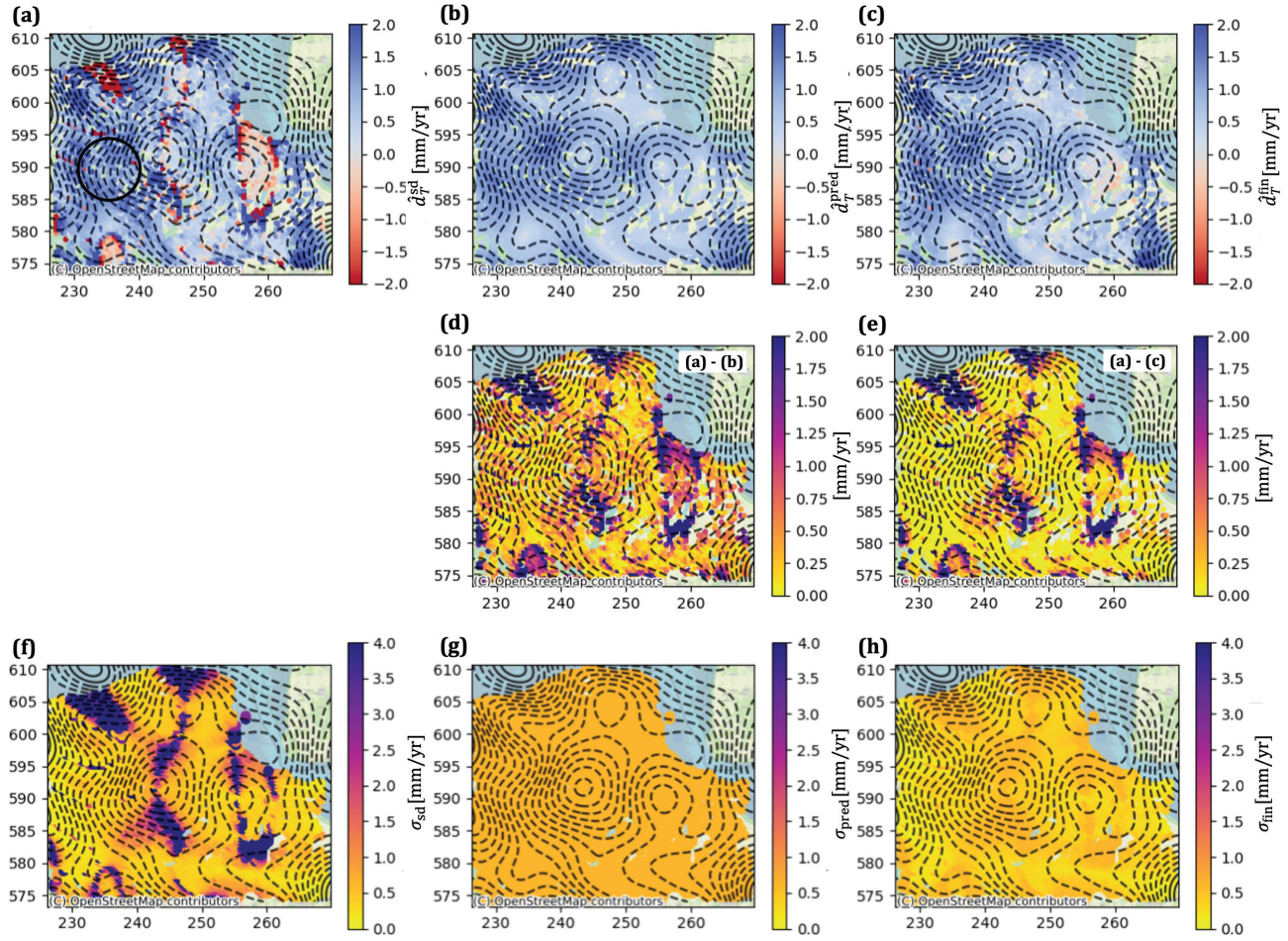

Figure 9. (a) Transversal velocities estimated using only the strapdown decomposition, $\hat{d}_T^{\text{sd}}$. Note that the colour bar is clipped. Corresponding quality values (σ) are shown in (f). (b) presents the results obtained via kriging interpolation, $\hat{d}_T^{\text{pred}}$, with corresponding sigmas in (g), and the difference with the strapdown results in (d). In (c), we show the combined estimates for the transversal component, $\hat{d}_T^{\text{fin}}$, derived by solving the mathematical model from Equations (13) and (14), with the associated σ values shown in (h), and the difference with the strapdown solution in (e). Notably, the combined approach improves the quality of the estimates – particularly for RUMs where the transversal direction aligns with the north–south direction; see the lower sigma values of (h) compared to (f). The circle in (a) locates the city of Groningen. RUM: region of uniform motion.

$$E\{\underbrace{\begin{bmatrix}\hat{d}_N^{\text{sd}}\\ \hat{d}_N^{\text{pred}}\end{bmatrix}}_{y}\} = \underbrace{\begin{bmatrix}1\\1\end{bmatrix}}_{A} d_N^{\text{fin}}, \text{ and} \tag{13}$$

$$D\{\underbrace{\begin{bmatrix}\hat{d}_N^{\text{sd}}\\ \hat{d}_N^{\text{pred}}\end{bmatrix}}_{y}\} = \underbrace{\begin{bmatrix}\sigma^2_{\hat{d}_N^{\text{sd}}} & 0\\ 0 & \sigma^2_{d_N^{\text{pred}}}\end{bmatrix}}_{Q_y}, \tag{14}$$

where d_N^{fin} is the final normal displacement velocity. The results for $\hat{d}_N^{\text{pred}}$ and d_N^{fin} and their corresponding variances are shown in Figures 8b, c, g, and h, respectively.

Figures 8d and e present the differences for $\hat{d}_N^{\text{pred}}$ and d_N^{fin} with the estimated velocities from the (kinematic) strapdown decomposition (see Section 3.2). It shows that $\hat{d}_N^{\text{pred}}$ is spatially smooth, with uniform standard deviation (σ) values for all RUMs. The differences between the predicted and the strapdown velocities show that significant differences occur primarily for the RUMs where the sigma value for the normal velocity was large.

Comparing the final estimates and their associated variances (see Figures 8c and h), it is clear that for the RUMs that had an unfavourable TLN frame orientation, the final velocities strongly converge towards the velocities obtained from the kriging interpolation. Conversely, for RUMs that had a trustworthy normal velocity, we see a minimal change, with final values relying more on the estimated values from the strapdown decomposition.

Transversal component

An analogous approach is followed for the transversal velocities. Similarly to normal velocities, the transversal component also exhibits spatial smoothness. However, its magnitude is more strongly correlated with the gradient of the subsidence bowl (Kratzsch, 1983). Therefore, rather than weighting RUMs by spatial distance in the kriging interpolation, weights are assigned based on *gradient differences*. To derive the corresponding kriging weights, we again computed a variogram, shown in Figure 11b, where the x-axis of the variogram represents the gradient difference between RUMs. We fitted a linear model with a nugget value of 0.45 mm²/yr² and a slope of $8.6 \cdot 10^8$ mm²/yr²/km. The variogram model is used to determine the weights

https://doi.org/10.70712/NJG.v105.13223

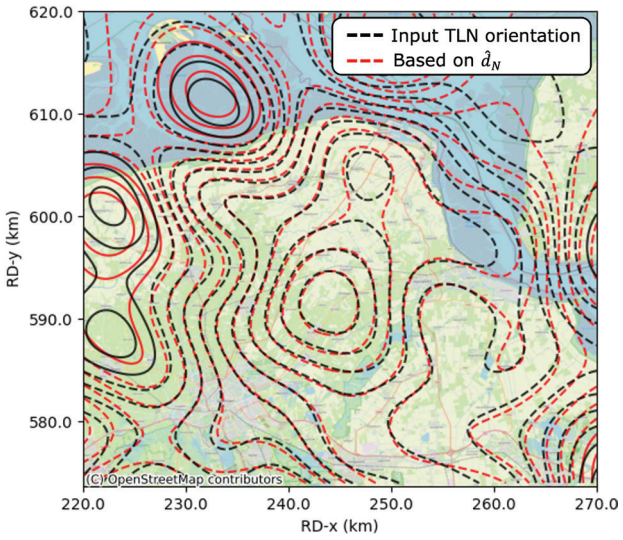

Figure 10. Contour lines that served as an input for the strapdown decomposition are shown in black, and the contour lines that were estimated from the normal component are shown in red. It can be seen that the input orientation of the TLN frame was rather good since the orientation of the two contour lines is almost identical. We also estimated new values for Λ with the contour lines based on the estimated normal component and compared them to our initial input for the strapdown decomposition. This resulted in a mean difference of 0.08 degrees and σ of 8 degrees. TLN: transversal, longitudinal, and normal.

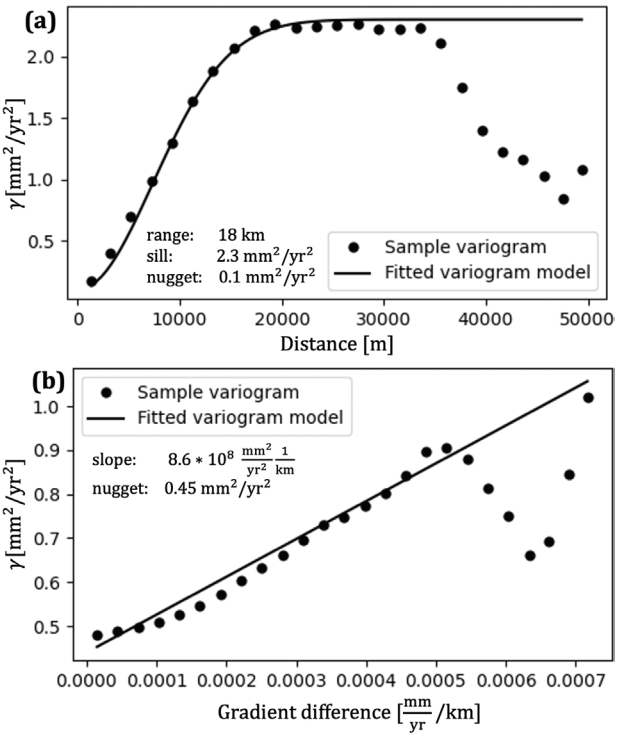

Figure 11. (a) shows the variogram of the **normal** deformation signal. The x-axis shows the range in meters. A Gaussian model was fitted to the variogram. Due to the bowl-shaped subsidence signal, the semivariance initially increases with distance. However, since the radius of the subsidence bowl is approximately 30 km, the semivariance decreases beyond 35 km. (b) shows the variogram of the *transversal* deformation signal, where we fitted a linear model. In this case, the range values represent differences in the gradient of the subsidence bowl rather than geometric distances. This reflects the expectation that RUMs on the same contour show a similar transversal deformation. RUM: region of uniform motion.

for the kriging interpolation (see Equation (12)), and subsequently to calculate the kriging velocities, as shown in Figure 9b.

As with the normal component, we estimate the final values for the transversal component using both the strapdown and kriging velocities, i.e. $\hat{d}_T^{\text{sd}}$ and $\hat{d}_T^{\text{pred}}$, respectively, using Equations (13) and (14) (see Figure 9c). For the 'poorly estimable RUMs', i.e. RUMs where the transversal direction is nearly aligned with the null line, we observe significant differences between the strapdown velocities and the final result. In these cases, the final estimate aligns closely with the kriging interpolation.

Considering both the transversal and normal components, we see a clear benefit from incorporating the smoothness of the signal, particularly for the poorly estimable RUMs. The extreme estimates (which are physically highly unlikely) and the high sigma values have significantly decreased. The RUMs that already had precise estimates remain largely unchanged.

From 2D local to 3D global

With the estimated transversal and normal displacement velocities and the frame orientation defined by angles Λ, Φ, and Ω, we can transform the estimates in the TLN frame to east, north, and up components with

$$d_{\text{ENU}} = R_1 R_2 R_3 \, d_{\text{TLN}}, \tag{15}$$

where R_1, R_2, and R_3 are the rotation matrices with the angles of the TLN frame (see Brouwer and Hanssen 2024, Equations 3–5) and d_{TLN} is defined as $[d_T^{\text{fin}}, 0, d_N^{\text{fin}}]^T$. Consequently, the variance–covariance matrix of d_{ENU} is

$$Q_{d_{\text{ENU}}} = R_1 R_2 R_3 Q_{d_{\text{TLN}}} R_3^T R_2^T R_1^T, \tag{16}$$

where

$$Q_{d_{\text{TLN}}} = \begin{bmatrix} \sigma^2_{d_T^{\text{fin}}} & 0 & 0 \\ 0 & \sigma^2_{d_L^{\text{fin}}} & 0 \\ 0 & 0 & \sigma^2_{d_N^{\text{fin}}} \end{bmatrix} = \begin{bmatrix} \sigma^2_{d_T^{\text{fin}}} & 0 & 0 \\ 0 & (d_T^{\text{fin}})^2 \sigma^2_{\Lambda} & 0 \\ 0 & 0 & \sigma^2_{d_N^{\text{fin}}} \end{bmatrix}. \tag{17}$$

For the value for $\sigma^2_{d_L^{\text{fin}}}$, we refer to Brouwer and Hanssen (2024, Figure 6). Obviously, while $Q_{d_{\text{TLN}}}$ is considered a diagonal matrix, the datum transformation results in $Q_{d_{\text{ENU}}}$ being a full matrix, where the non-zero covariance terms describe the orientation and shape of the 3D confidence ellipsoid. As the frame orientation differs per RUM, the transformation must be applied per RUM.

Comparison with GNSS

To validate the results, the estimated InSAR displacements are compared with estimated Global Navigation Satellite System (GNSS) displacements of more than 30 continuous Global

https://doi.org/10.70712/NJG.v105.13223

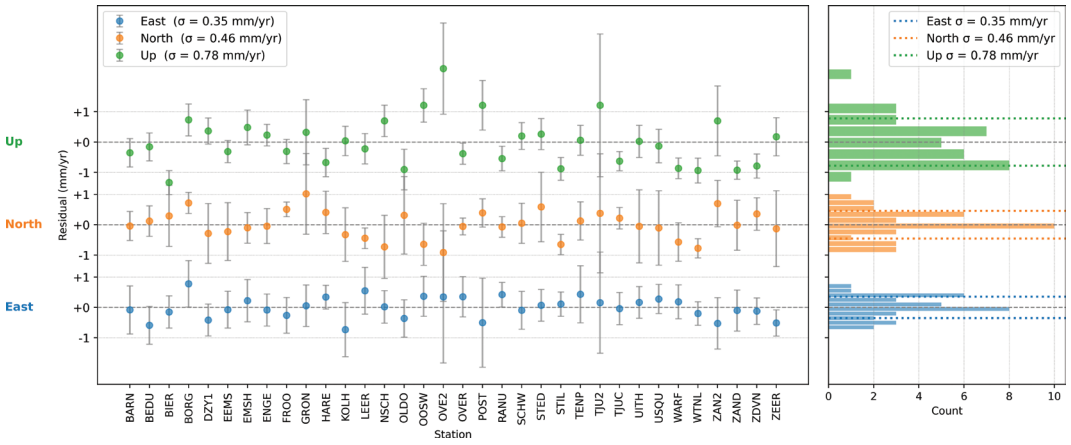

Figure 12. Residuals between InSAR and GNSS velocity estimates for each GNSS station, after applying the correction to obtain both estimates in the ETRF89 reference frame. The residuals are shown for the east, north, and up components shown in blue, orange, and green, respectively. In the right panel, the corresponding histograms are shown, where the residuals are approximately normally distributed, with standard deviations of $\sigma E = 0.35$ mm/yr, $\sigma N = 0.46$ mm/yr, and $\sigma U = 0.78$ mm/yr, for the east, north and up components, respectively. As the values are small, this yields confidence in the reliability of the InSAR-derived velocities.

Positioning System (GPS) stations that have been installed to continuously monitor ground displacements. For each GNSS station, the east-north-up (ENU) GNSS velocity is compared to the Interferometric SAR (InSAR) ENU velocity that corresponds to the RUM hosting the GNSS station. The differences between the two estimates are computed as

$$\Delta d_i^{I\to E} = \hat{d}_i^{G|E} - \hat{d}_i^{I} \tag{18}$$

where $\hat{d}_i^{G|E}$ denotes the displacement velocity of a GNSS station (superscript G) situated in RUM i, expressed in the ETRF89 reference frame (superscript E), while $\hat{d}_i^{I}$ represents the estimated InSAR velocity (superscript I) for the same RUM (Lapadat et al., 2025). Note that the InSAR velocities are inherently estimated relative to an InSAR reference point, which is located outside the gas production area. The InSAR-derived velocities can be expressed with respect to the ETRF89 reference frame as well, by applying a correction to the estimated InSAR velocities. If $\Delta d_i^{I\to E} \neq 0$, the estimated offset $\Delta d_i^{I\to E}$ can be added to the InSAR velocities to align them with ETRF89. This procedure needs to be performed independently for each displacement component. After computing the differences between the GNSS velocities and the InSAR velocities in these RUM grid cells, we retrieved $\Delta d_i^{I\to E}$ for each directional component: $\Delta d_{i,\text{east}}^{I\to E} = -0.16$ mm/yr, $\Delta d_{i,\text{north}}^{I\to E} = -0.05$ mm/yr, and $\Delta d_{i,\text{up}}^{I\to E} = 0.78$ mm/yr for the east, north, and up components, respectively.

In Figure 12, we show the differences between the estimated InSAR and GNSS velocities for the east, north, and up components after correction for the offsets. Additionally, we show the histograms of the residuals. This shows that the residuals are approximately normally distributed, with relatively small standard deviations, i.e. $\sigma_E = 0.35$ mm/yr, $\sigma_N = 0.46$ mm/yr, and $\sigma_U = 0.78$ mm/yr. As the values are small, this yields confidence in the reliability of the InSAR-derived velocities.

Results

Combining the results of both the transversal and normal components into a single final product (see Figure 13) provides a 3D representation of the displacement field over

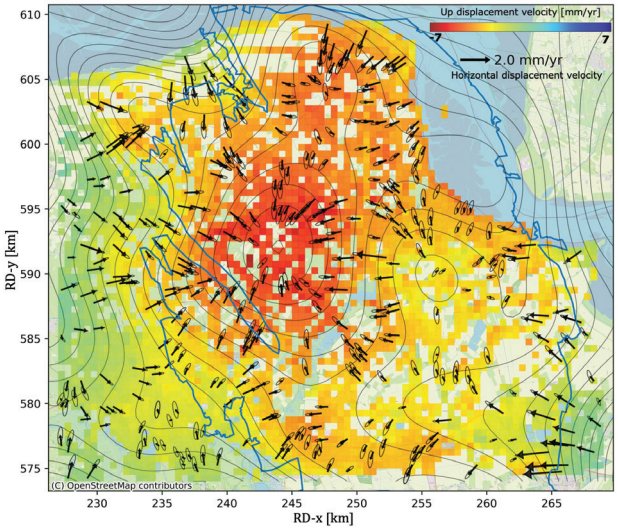

Figure 13. Estimated 3D displacement velocities over Groningen using the two InSAR viewing geometries and the strapdown approach. The outline of the reservoir is shown by the blue line. The colours in the background and the contour lines correspond to the vertical direction. The maximum vertical (up) velocities occur in the centre of the field and reach values up to 6.5 mm/yr. The black vectors represent the horizontal direction, and the ellipses the corresponding 2σ confidence regions. At the edges of the field, where contour lines are closer together, the estimated horizontal velocities are largest.

Groningen, expressed in the ETRF89 reference frame. The background colours and contour lines represent the estimated up velocities, with maximum values occurring near the centre of the field, reaching up to 6.5 mm/yr at [53.30705°N, 6.72238°E] (ETRF89), near the village of Ten Post. A local maximum of 6.1 mm/yr is found at coordinates [53.28713°N, 6.88673°E], ~6 km SSW of Delfzijl. Note that the precision of the up component $\sigma_{d_u}^2$ is computed for every grid cell, but not visualised in Figure 13.

The black vectors show the estimated horizontal motion, and surrounding ellipses indicate corresponding 2σ confidence regions of the estimates. While directional horizontal motion is estimated for every coloured 500 × 500 m grid cell in the image, only a random subset of 10% of the actual vectors is displayed to avoid clogging the image. At the edges of the field, where the

https://doi.org/10.70712/NJG.v105.13223

contour lines are denser, the estimated horizontal velocities are larger, as would be expected from theory (Kratzsch, 1983). Unlike the initial output from the strapdown decomposition, the estimated directional and magnitude precision is now more uniform across the entire field, with realistic estimates varying over the sectorial position. We observe maximum horizontal displacements around the village of Bedum, ~9 km NNE of Groningen city.

Expressing the estimated displacements with their east, north, and up components, the quality of these estimates is described with a full 3 × 3 variance–covariance matrix. The dataset corresponding to this result has been made publicly available (see Brouwer and Hanssen 2025). For the centroid of each RUM, the estimated displacement velocities in the east, north, and up directions are provided, along with their associated uncertainties, in terms of variances and covariances. This results in a total of nine parameters per RUM: three velocities: d_e, d_n, d_u; three variances: $\sigma^2_{d_e}, \sigma^2_{d_n}, \sigma^2_{d_u}$; and three covariances: $\sigma_{d_e,d_n}, \sigma_{d_e,d_u}, \sigma_{d_n,d_u}$. With these results, it is possible to run inverse models or predict future positions.

Discussion

The reported results depend on several assumptions and methodological choices. The analysis is based on estimated mean velocities assuming a steady-state deformation model. Consequently, potential temporal variations or changes in deformation behaviour are not explicitly accounted for, and may bias the results. Obviously, the results should be interpreted within the analysed time interval (2015–2023) and are not valid outside this period.

The decomposition is based on the assumption that we successfully isolated InSAR displacements that are driven by the gas extraction, and therefore relies on a sufficiently good classification. This classification of scatterers into deep-only and mixed classes is defined by smoothness constraints, both during the initial quadtree classification and the subsequent reclassification steps, and depends on particular chosen thresholds. The classification may also fail when a RUM contains a single dominant deformation pattern, such as a railway. The subsequent reclassification steps help mitigate such cases, although the second reclassification additionally depends on variogram parameters used to predict the deep signal at the location of mixed scatterers. Importantly, all these assumptions and thresholds have been explicitly defined, making their influence transparent and open to scrutiny.

The performance of the decomposition itself depends on the spatial discretisation into RUMs and on having sufficient observations from both viewing geometries within each RUM. RUMs over water or decorrelated areas may not contain enough observations to provide reliable estimates, which is reflected by the gaps in the final result. To account for this, the quality of the estimated mean velocity (per RUM) is explicitly propagated into the decomposition, such that a lower number of observations is reflected in a larger uncertainty. Finally, we assume no spatial correlation between the estimated parameters of different RUMs, resulting in a diagonal Q^x. This is considered a reasonable assumption because each RUM contains unique scatterers whose observations are described by their own stochastic model.

Conclusion

This study provides the first estimation of the full three-dimensional displacement field in Groningen resulting from gas extraction, derived from InSAR observations using the strapdown method, and accompanied by a detailed quality assessment. The approach is data-driven, but incorporates falsifiable prior knowledge on the expected smoothness of the deformation signal caused by the gas extraction at multiple stages of the analysis. The assumed smoothness of the deep deformation component allows us to classify scatterers into two distinct classes. The *deep-only* classified scatterers are isolated and used in the strapdown decomposition. We have shown that the local frame orientation can be estimated directly from satellite LoS data to a sufficient degree of precision. The strapdown approach propagates the associated orientation uncertainties to take them into account in the estimation and quality assessment of the final displacement parameters.

Using the RUMs where the precision for the estimated transversal and normal velocities is good, it is possible to provide smoothness constraints that can, in turn, be used to improve displacement estimates for RUMs where the initial strapdown estimates were poor.

As a result, we obtain reliable estimates for the displacements across the entire province of Groningen during the period 2015–2023, with a maximum subsidence velocity of 6.5 mm/yr, and directional horizontal displacements induced by gas extraction, which are significant, up to 1.8 mm/yr. For 50% of the analysed area, the estimated horizontal displacements are greater than twice the standard deviation of the estimator. In other words, for half of the area we can derive a statistically significant estimate of the horizontal component.

Acknowledgements

This research is part of the DeepNL project and is supported by the Dutch Research Council (NWO), grant no.: DEEPNL.2018.052. We acknowledge SkyGeo for support and for providing the radar interferometric data. Sentinel-1 data were provided by the European Space Agency (ESA).

References

Brouwer, W.S. & Hanssen, R.F., 2023. A treatise on InSAR geometry and 3-D displacement estimation. IEEE Transactions on Geoscience and Remote Sensing **61**: 1–11. DOI: 10.1109/TGRS.2023.3322595

Brouwer, W.S. & Hanssen, R.F., 2024. Estimating three-dimensional displacements with InSAR: the strapdown approach. Journal of Geodesy **98**: 1–15. DOI: 10.1007/s00190-024-01918-2

Hanssen, R. Brouwer, W., 2025. 3D displacement estimates due to deep-seated hydrocarbon production in Groningen from satellite radar interferometry, 2015-2023. Version 1. 4TU.ResearchData. dataset. https://doi.org/10.4121/34394aab-6139-4397-9235-f9f041ac9299.v1

Finkel, R.A. & Bentley, J.L., 1974. Quad trees a data structure for retrieval on composite keys. Acta Informatica **4**: 1–9. DOI: 10.1007/BF00288933

Fokker, P.A., Van Leijen, F.J., Orlic, B., Van Der Marel, H. & Hanssen, R.F., 2018. Subsidence in the Dutch Wadden sea. Netherlands Journal of Geosciences **97**(3): 129–181. DOI: 10.1017/njg.2018.9

Geertsma, J., 1973. Land subsidence above compacting oil and gas reservoirs. Journal of Petroleum Technology **25**(6): 734–744. DOI: 10.2118/3730-PAq

Hanssen, R.F., 2001. Radar interferometry: data interpretation and error analysis. Springer Dordrecht, DOI: 10.1007/0-306-47633-9

Hanssen, R.F. & van Leijen, F.J., 2017. Bodemdalingskaart Nederland, geodetische analyse. Accessed 25 September 2024. https://bodemdalingskaart.nl/en-us/kennis-datacentrum/

Hu, F., Wu, J., Chang, L. & Hanssen, R.F., 2019. Incorporating temporary coherent scatterers in multi-temporal InSAR using adaptive temporal subsets. IEEE Transactions on Geoscience and Remote Sensing **57**(10): 7658–7670. DOI: 10.1109/TGRS.2019.2915658

Huber, P.J., 2011. Robust Statistics. In M. Lovric (Eds.), International Encyclopedia of Statistical Science. Springer, Berlin, Heidelberg. https://doi.org/10.1007/978-3-642-04898-2_594

Ketelaar, G., Bähr, H., Liu, S., Piening, H., van der Veen, W., Hanssen, R., van Leijen, F., van der Marel, H. & Samiei-Esfahany, S., 2020. Integrated monitoring of subsidence due to hydrocarbon production: consolidating the foundation. Proceedings of the International Association of Hydrological Sciences **382,** 117–123. DOI: 10.5194/piahs-382-117-2020

Ketelaar, G., van Leijen, F., Marinkovic, P. & Hanssen, R., 2006. On the use of point target characteristics in the estimation of low subsidence rates due to gas extraction in Groningen, The Netherlands. In A. Arnaud & J. Mallorquí (Eds.), Proceedings of the Fringe 2005 Workshop, Frascati, Italy, 28 November–2 December 2005 (ESA SP-610). Noordwijk: ESA Publications Division.

Ketelaar, V.B.H., 2009. Satellite radar interferometry: Subsidence monitoring techniques. Remote Sensing and Digital Image Processing, Vol. 14. Springer, Dordrecht. DOI: 10.1007/978-1-4020-9428-6

Kim, S.S.R., 2025. Data assimilation for subsidence analysis of the Groningen region: A multi-scale study with importance sampling. [Dissertation (TU Delft), Delft University of Technology]. https://doi.org/10.4233/uuid:610bb429-08c8-4870-8194-72b0ea1c7c97

Kratzsch, H., 1983. Mining subsidence engineering. Springer Science & Business Media, Heidelberg. DOI: 10.1007/978-3-642-81923-0

Lapadat, A.M., Andreas, H., Brouwer, W.S., van Diepen, S., Pradipta, D. & Hanssen, R., 2025. Land subsidence in Jakarta in three dimensions (2014–2025) using InSAR-GNSS datum connection and the strapdown decomposition. Preprint, EarthArXiv, Version 4, Accessed 23 October 2026. DOI: 10.31223/X5R45H

NAM, 2015. Bodemdaling door Aardgaswinning: NAM gasvelen in Groningen, Friesland, en het noorden van Drenthe. Status Rapport 2015 en Prognose tot het jaar 2080. NAM rapport nr. 201511213444. Nederlandse Aardolie Maatschappij B.V. [in Dutch].

NAM, 2020. Bodemdaling door aardgaswinning – statusrapport 2020 en prognose tot het jaar 2080 (December 2020). Accessed 13 November 2026. https://www.nam.nl/veiligheid-milieu/bodemdaling-door-gaswinning.html#iframe=L3JlcG9ydHMvc3 ViamVjdC9ib2RlbWRhbGluZy8jLw%3D%3D

Qin, Y., Salzer, J., Maljaars, H. & Leezenberg, P.B., 2019. High resolution InSAR in the Groningenarea 2018–2019 advanced services. Technical report. NAM, SkyGeo. Accessed 19-11-2026. https://nam-onderzoeksrapporten.data-app.nl/reports/download/groningen/en/26e6a722-b7c2-4fc1-a877-38066df51f14

Samet, H., 1984. The quadtree and related hierarchical data structures. ACM Computing Surveys (CSUR) **16**(2): 187–260. DOI: 10.1145/356924.356930

Schreuder, W., Busscher, N., Postmes, T., Zijlstra, A. & Vojvodic, E., 2023. Insight into impact: the societal consequences of gas extraction in Groningen and ways of thinking for the Future. Kennisplatform Leefbaar en Kansrijk Groningen. 125 p.

van der Voort, N. & Vanclay, F., 2015. Social impacts of earthquakes caused by gas extraction in the province of Groningen, the Netherlands. Environmental Impact Assessment Review **50**: 1–15. DOI: 10.1016/j.eiar.2014.08.008

van der Lee, T., 2023. Groningers boven gas: Eindrapport van de parlementaire enquˆetecommissie aardgaswinning groningen. Accessed 13 November 2026. https://www.tweedekamer.nl/Groningen/rapport

van Eijs, R.M. & van der Wal, O., 2017. Field-wide reservoir compressibility estimation through inversion of subsidence data above the Groningen gas field. Netherlands Journal of Geosciences **96**(5): s117–s129. DOI: 10.1017/njg.2017.30

van Thienen-Visser, K. & Fokker, P.A., 2017. The future of subsidence modelling: compaction and subsidence due to gas depletion of the Groningen gas field in the Netherlands. Netherlands Journal of Geosciences **96**(5): s105–s116. DOI: 10.1017/njg.2017.10

van Thienen-Visser, K., Pruiksma, J. & Breunese, J., 2015. Compaction and subsidence of the Groningen gas field in the Netherlands. Proceedings of the International Association of Hydrological Sciences **372**: 367–373. DOI: 10.5194/piahs-372-367-2015